

See discussions, stats, and author profiles for this publication at: <https://www.researchgate.net/publication/234991885>

# Effects of density on the local dynamics and conformational statistics of polyethylene: A molecular dynamics study

ARTICLE *in* THE JOURNAL OF CHEMICAL PHYSICS · MAY 2000

Impact Factor: 2.95 · DOI: 10.1063/1.481472

---

CITATIONS

19

---

READS

9

3 AUTHORS, INCLUDING:



[Konstantinos Karatasos](#)

Aristotle University of Thessaloniki

64 PUBLICATIONS 1,204 CITATIONS

SEE PROFILE

# Effects of density on the local dynamics and conformational statistics of polyethylene: A molecular dynamics study

K. Karatasos,<sup>a)</sup> D. B. Adolf,<sup>b)</sup> and S. Hotston

*Department of Physics and Astronomy, University of Leeds, Leeds, United Kingdom*

(Received 28 December 1999; accepted 24 February 2000)

Molecular dynamics simulations of united atom (UA) linear polyethylene were performed as a function of density, for systems of two well-separated chain lengths ( $N=20$ ,  $N=100$ ). The role of the exact shape of the torsional angle potential is investigated by invoking two commonly cited alkane torsional potentials [Ryckaert–Bellemans (R&B), Steele]. The increase in second-neighbor torsional angle coupling with increasing density and decreasing conformational transition rates is presented quantitatively for the first time. The simulated local orientational dynamics were also studied by means of geometric autocorrelation functions (ACFs). These ACFs were analyzed by a method that emphasizes the distribution of relaxational processes, thereby providing specific information on the relevant spectral characteristics of each process. For all densities and chain lengths studied, two peaks are observed that are well separated in time. Only for the longer chains at the highest density studied does a third intermediate peak develop. Further insight into density-induced changes to the local dynamics is obtained through the distribution of angular jumps which give rise to decay of the geometric ACFs. © 2000 American Institute of Physics. [S0021-9606(00)51119-2]

## I. INTRODUCTION

Efforts within the polymer community have highlighted the importance of the local static and dynamic conformational characteristics of amorphous flexible polymers to their overall performance and observed macroscopic properties. Local polymer dynamics on the length scale of a few repeat units are a composite of motional processes including bond length oscillations, valence angle flexing in addition to the conformational activity of torsional angles. A detailed understanding of this atomistic motion offers valuable insight into the manner in which a polymer backbone localizes the motion associated with its conformational events, thereby avoiding the huge friction resistance accompanying a long tail swinging through a solvent or a melt environment. An effective means of understanding how these motions are affected by a wide number of factors related to the polymer chain and its environment is available via computer simulation techniques. Several studies over the years have made important contributions in this general area. However, an understanding of how modifications to density and intramolecular connectivity quantitatively influence the configurational and motional characteristics of polymers on short scales is still unclear. This manuscript is to serve as a step in this direction where simulations are systematically carried out as a function of density, backbone length, or the form of the torsional angle potential while keeping all other simulation quantities unchanged. Polyethylene is chosen as the target polymer due to its structural simplicity and its technological importance.

The paper is organized as follows: Sec. II reviews the

details of the simulation method and relevant parameters. Static chain properties and conformational statistics are presented in Sec. III for validation purposes. Section III also contains a quantitative comparison of the torsional angle coupling as a function of density, chain length, and torsional angle parametrization. In Sec. IV, a detailed examination of the short-scale dynamic response in terms of the relaxation of local reorientational motions is presented, while a summary is given in Sec. V.

## II. SIMULATION DETAILS

### A. Starting configurations and trajectory details

An initial pool of chains was constructed via the cooperative motion algorithm (CMA),<sup>1–3</sup> which is a lattice Monte Carlo approach capable of operating at very high densities (i.e., at full occupation of the lattice sites). Several thousands of chains of length 20 or 100 united atom CH<sub>2</sub> groupings (UA) were placed on a face-centered cubic lattice and allowed to move under strictly cooperative rearrangements. The runs were performed in the athermal limit where all attempted moves which avoid monomer–monomer overlaps are accepted, preserving at the same time the chain connectivity and the bond lengths. During the equilibration period the center of mass of each chain has diffused over a distance of several radii of gyration, while both the short and long length-scale modes were completely relaxed. Figure 1 plots the autocorrelation functions (ACFs) of the *bond* (**b**) [ $C_b(t) = \langle [\mathbf{b}(0) \cdot \mathbf{b}(t)] / [b^2(0)] \rangle$ ] and *end-to-end* (**R<sub>ee</sub>**) [ $C_{ee}(t) = \langle [\mathbf{R}_{ee}(0) \cdot \mathbf{R}_{ee}(t)] / [R_{ee}^2(0)] \rangle$ ] vectors as a function of the CMA step number per monomer. The bond ACF is observed to decay the fastest followed by the end-to-end vector ACFs for a 20-unit chain and for a 100-unit chain. A subset of chains from these pools was brought to the desired

<sup>a)</sup>Electronic mail: Kkaratas@ulb.ac.be

<sup>b)</sup>Electronic mail: D.B.Adolf@leeds.ac.uk

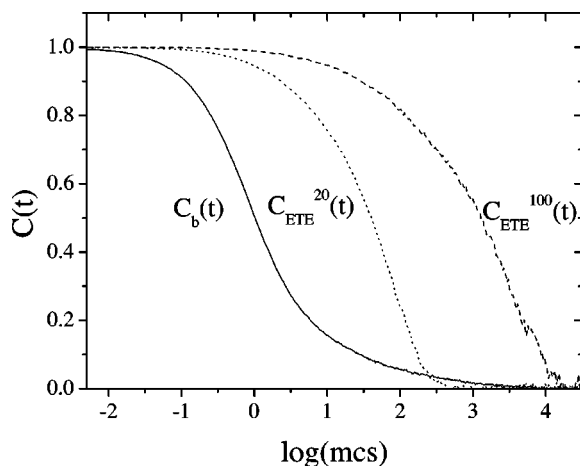


FIG. 1. The autocorrelation functions for the monomer (solid line), and the end-to-end vectors for the  $N=20$  (dotted line) and the  $N=100$  (dashed line) chain systems. Superscripts refer to the number of monomers of the corresponding chain model. The time units are expressed in Monte Carlo steps per monomer (mcs).

density by translating the chains towards this subset's center of mass in small steps to avoid overlaps. During this contraction, bond lengths and valence angle constraints were imposed on the selected chains. This process was used to generate six starting configurations for the molecular dynamics (MD) simulations, comprised of 50 chains of 20 united atoms (i.e., 50/20) and 10 chains of 100 united atoms (i.e., 10/100) at three different densities as summarized in Table I.

The MD simulation runs were performed in two stages. First, starting configurations were subjected to a 4 ns NVT equilibration period at 400 K using the Nosé–Hoover algorithm<sup>4</sup> with a characteristic thermostat relaxation time of 0.1 ps. Each 4 ns NVT simulation was followed by an 18 ns trajectory within the NVE ensemble with configurations stored every 1 ps. Static quantities such as  $\langle R_{ee} \rangle$  and  $\langle R_g \rangle$ , where  $R_g$  denotes the radius of gyration, in addition to dynamic quantities such as conformational activity and various correlation functions for these systems, are discussed in Secs. III and IV, respectively, as a function of density. The reproducibility of these quantities was confirmed through the use of different 50/20 and 10/100 starting configurations.

### B. Simulation parameters

The simulations discussed in this manuscript were performed through the DL\_POLY molecular dynamics package.<sup>5</sup> The integration of the equation of motion is based on the

Verlet leapfrog scheme<sup>6</sup> using a 2 fs time step. The united atoms groupings are connected together with rigid bonds of length  $l_0 = 1.53 \text{ \AA}$  using the SHAKE algorithm.<sup>7</sup> The valence angle potential is of harmonic cosine form

$$\Phi(\theta) = \frac{1}{2}k_\theta(\cos\theta - \cos\theta_0)^2, \quad (1)$$

where  $k_\theta = 124.2 \text{ kcal/mol}$  and  $\theta_0 = 112.813^\circ$ . For the restriction of the torsional angle rotation, simulations were performed using either the expression due to Steele<sup>8</sup> or the expression due to Ryckaert & Bellemans (R&B).<sup>9</sup> Both expressions are of the form

$$V(\phi) = \sum_{i=0}^n a_i \cos^i \phi, \quad (2)$$

where  $n=3$  for the Steele potential and  $n=5$  for the R&B expression. The relative parameters are given in Table II, while Fig. 2 depicts the form of each potential between  $\pm 180 \text{ deg}$ . Distinct features characterizing the two potentials are the significantly different  $g^+ \leftrightarrow g^-$  barrier height, the moderately larger  $g \leftrightarrow t$  barrier of the Steele potential, as well as the different locations of their *gauche* minima.

The nonbonded interactions between two united atoms  $i$  and  $j$  separated by a distance of  $r_{ij}$  are modeled by a Lennard-Jones potential

$$U(r_{ij}) = 4\epsilon \left[ \left( \frac{\sigma}{r_{ij}} \right)^{12} - \left( \frac{\sigma}{r_{ij}} \right)^6 \right], \quad (3)$$

with  $\epsilon = 0.1132 \text{ kcal/mol}$ ,  $\sigma = 4.28 \text{ \AA}$ , and a cutoff distance  $r_c$  of  $7 \text{ \AA}$ . Intramolecular nonbonded interactions are computed when  $i$  and  $j$  are separated by no less than four bonds.

### III. STATIC PROPERTIES

Several static properties were analyzed as a means of validating the output of the simulations. Table III summarizes the mean square of the end-to-end vector  $\langle R_{ee}^2 \rangle$  and the radius of gyration  $\langle R_g^2 \rangle$  of the simulated systems, together with their ratio  $\Lambda = \langle R_{ee}^2 \rangle / \langle R_g^2 \rangle$  as calculated by averaging over all the chains and over the production phase of each simulation. The observed chain dimensions compare well to results reported from recent simulation efforts<sup>10–13</sup> for similar models.

The  $\Lambda$  values for the 50/20 systems are seen to be consistently higher for systems using the Steele torsional angle potential energy expression compared to their R&B counterparts. In contrast, there is no similar systematic trend for the 10/100 systems.

Figure 3 shows a comparison of the form factor of the 10/100 systems for the Steele potential calculated from the simulation trajectories using the expression

$$S(q) = \frac{1}{N} \left\langle \sum_{ij}^N \frac{\sin q r_{ij}}{q r_{ij}} \right\rangle, \quad (4)$$

where  $N$  is the number of united atom groupings per chain,  $r_{ij}$  is the distance between the  $i$ th and the  $j$ th bead belonging to the same chain, and  $q$  is the magnitude of the scattering vector. The angular brackets refer to an average over all

TABLE I. Characteristics of the simulated systems.

Code	Density g/cm <sup>3</sup>	Number of chains	Chain length	Torsional potential
$S_1$	0.29	50	20	Steele, (Ref. 8) R&B (Ref. 9)
$S_2$	0.59	50	20	Steele, R&B
$S_3$	0.70	50	20	Steele, R&B
$L_1$	0.29	10	100	Steele, R&B
$L_2$	0.59	10	100	Steele, R&B
$L_3$	0.79 <sup>a</sup>	10	100	Steele, R&B

<sup>a</sup>Accounts for bulk polyethylene density at  $T=400 \text{ K}$  (Ref. 53).

TABLE II. Parameters for the torsional potential expressions in kcal/mol.

	$a_0$	$a_1$	$a_2$	$a_3$	$a_4$	$a_5$	$t \rightarrow g$ barrier	$\Delta \theta_{t \rightarrow g}$ (deg)
Steele	2.1095	4.3200	1.1658	-7.593			2.55	112.7
R&B	2.2163	2.9035	-3.1338	-0.7308	6.2677	-7.5229	2.24	120

chains and over the entire production phase of a simulation. The lines within this figure are calculated using the Debye formula  $g(q)$  for Gaussian coils.<sup>14</sup>

$$g(q) = \frac{2N}{(qR_g)^4} (e^{-(qR_g)^2} + (qR_g)^2 - 1), \quad (5)$$

where the respective  $R_g$  values were substituted by the averages calculated from the simulations (see Table III). As shown, the low  $q$  regime of the computed  $S(q)$  agrees well with the Debye function, implying Gaussian behavior on long length scales for the 10/100 models. The same level of agreement was observed for the analogous systems simulated with the R&B potential. Due to the short chain length, the 50/20 systems do not exhibit Gaussian behavior, even for the lower  $q$  range.

### A. Conformational statistics: Transition rates and cooperativity

Previous studies on several polymeric systems including isolated chains, phantom chains, chains in solution, and bulk chains have provided rather fragmented information on the effects of the respective local environment on the short-scale conformational behavior.<sup>15–27</sup> In the following sections, a systematic investigation of the cooperative nature of the conformational transitions and the associated transition rates is presented, as a function of density (from rarified to bulk systems), chain length, and form of the torsional angle potential. In addition, in order to assess the effects of the definition of a transition on the conformational statistics (as different definitions are frequently encountered in the literature,<sup>15,16,27,28</sup>) two characteristic cases are examined. Case A defines a transition as the first time a torsional angle, that starts within a  $\pm 20$  deg window of one of the torsional angle potential energy minima in Fig. 2, rotates within  $\pm 20$

deg window of a neighboring minima. The selected well width of  $\pm 20$  deg is slightly larger than a  $k_B T$  oscillation ( $k_B$  is the Boltzmann's constant) at 400 K for either the Steele or the R&B torsional potentials. Definition B is based on the work of Helfand,<sup>28</sup> where a transition is defined as the first time a torsional angle rotates from the vicinity of the minima of one of the torsional angle potential energy wells to the minimum of a neighboring well.

### 1. Transition rates

The conformational rates of isolated polyethylene (PE) chains modeled with intramolecular nonbonded interactions have been reported to be very similar to the jump rates of isolated chains under phantom conditions, but higher than the transition rates observed in the bulk.<sup>15</sup> In a polyisoprene (PI) model a comparative study of systems under solution and vacuum states showed that the average time between conformational transitions was similar.<sup>16</sup> For the melt, similar transition rates were observed, though at a temperature 115 K higher than the other states.

For the PE models (Table I) examined in the present work, Figs. 4(a), 4(b), 5(a), and 5(b) summarize the densification effect on the average number of transitions per torsional angle per picosecond (definition B) for each Steele and R&B torsional angle within the 50/20 and the 10/100 systems, respectively. The transition rates are represented as open symbols. The filled symbols within Figs. 4 and 5 depict the “signed” analogs of the corresponding open symbols where transitions are assigned as positive or negative, depending on whether their rotation is clockwise or counter-clockwise. Clockwise is defined as moving from left to right in Fig. 2. Lines are drawn as aids to the eye.

The unsigned transition rates reveal that the four or five torsional angles from the chains ends within each system simulated illustrate an enhanced transition rate relative to transition rates for torsional angles within the interior of the chain. This effect is present at all densities and is the well-known increase of reorientational freedom present at the

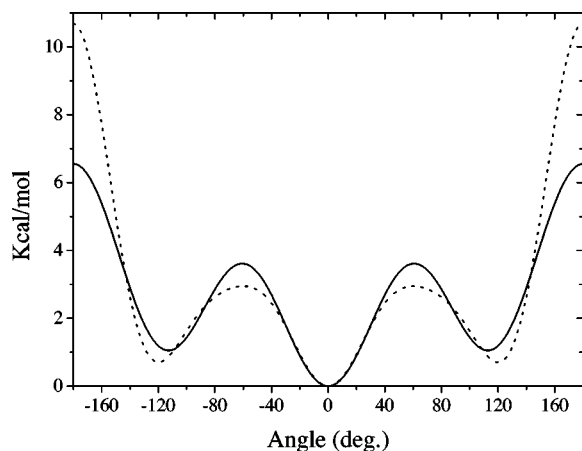


FIG. 2. The Steele (solid curve) and Ryckaert & Bellemans (R&B, dotted curve) torsional potentials.

TABLE III.  $\langle R_{ee}^2 \rangle$ ,  $\langle R_g^2 \rangle$  and their ratio  $\Lambda = \langle R_{ee}^2 \rangle / \langle R_g^2 \rangle$  for the simulated systems.

System	Steele			R&B		
	$\langle R_{ee}^2 \rangle / \text{\AA}^2$	$\langle R_g^2 \rangle / \text{\AA}^2$	$\Lambda$	$\langle R_{ee}^2 \rangle / \text{\AA}^2$	$\langle R_g^2 \rangle / \text{\AA}^2$	$\Lambda$
$S_1$	$328 \pm 12$	$37 \pm 1$	8.8	$305 \pm 12$	$37 \pm 1$	8.2
$S_2$	$337 \pm 12$	$38 \pm 1$	8.9	$313 \pm 11$	$38 \pm 1$	8.2
$S_3$	$353 \pm 13$	$41 \pm 1$	8.6	$320 \pm 12$	$39 \pm 1$	8.2
$L_1$	$2563 \pm 370$	$375 \pm 33$	6.8	$2214 \pm 290$	$323 \pm 33$	6.8
$L_2$	$2741 \pm 350$	$400 \pm 35$	6.8	$2575 \pm 359$	$363 \pm 32$	7.1
$L_3$	$2532 \pm 196$	$351 \pm 19$	7.2	$2684 \pm 334$	$382 \pm 29$	7.0

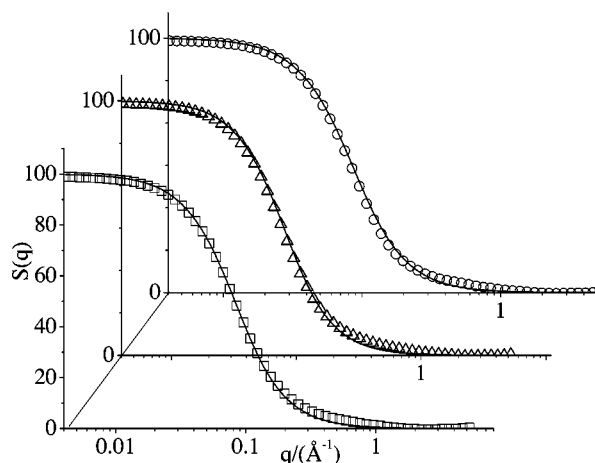


FIG. 3. Comparison of the form factor for the 10/100 systems simulated with the Steele torsional potential to the respective Debye expression for chains of the same length and radii of gyration:  $\square$   $\rho=0.29$  g/cm<sup>3</sup>,  $\triangle$   $\rho=0.59$  g/cm<sup>3</sup>,  $\circ$   $\rho=0.79$  g/cm<sup>3</sup>.

chain ends. In order to avoid any possible bias, the end torsional angles are not included in the estimation of average backbone transition rates discussed hereafter.

For a given torsional angle expression, the unsigned transition rates for the 50/20 and the 10/100 systems are observed to gradually decrease as the density is increased. Absolute values of the transition rates are rather insensitive to the chain lengths examined. When switching from transi-

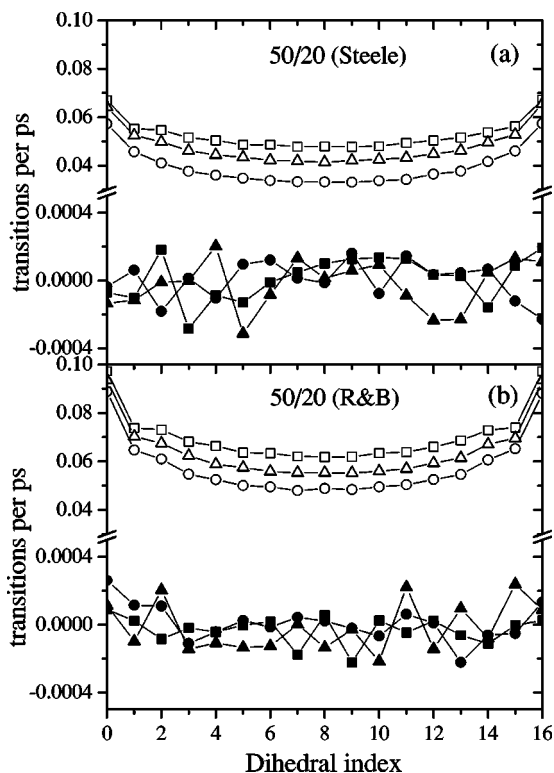


FIG. 4. Transition rates in ps<sup>-1</sup> for the 50/20 models, at all the examined densities ( $\square$ ,  $\blacksquare$   $\rho=0.29$  g/cm<sup>3</sup>,  $\triangle$ ,  $\blacktriangle$   $\rho=0.59$  g/cm<sup>3</sup>,  $\circ$ ,  $\bullet$   $\rho=0.70$  g/cm<sup>3</sup>) in systems simulated with the Steele (a) and the R&B (b) torsional potentials, adopting definition B for the conformational transitions. The filled and open symbols represent the signed and the unsigned cases (see the text), respectively.

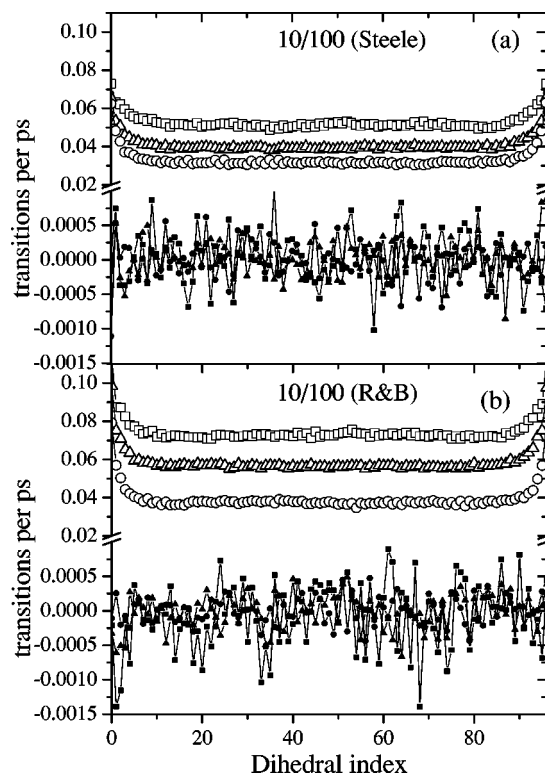


FIG. 5. Transition rates in ps<sup>-1</sup> for the 10/100 systems, at all the examined densities ( $\square$ ,  $\blacksquare$   $\rho=0.29$  g/cm<sup>3</sup>,  $\triangle$ ,  $\blacktriangle$   $\rho=0.59$  g/cm<sup>3</sup>,  $\circ$ ,  $\bullet$   $\rho=0.79$  g/cm<sup>3</sup>) in systems simulated with the Steele (a) and the R&B (b) torsional potentials, adopting definition B for the conformational transitions. The filled and open symbols represent the signed and the unsigned cases (see the text), respectively.

tion definition B to transition definition A, Tables IV and V reveal that B rates are lower than A rates by up to 40% for Steele and up to 50% for R&B models. The lower B rates emphasize the additional time required to cross a potential minima relative to that required to enter a region which starts  $\pm 20$  deg from a minima. For both definitions at all densities and for both the Steele and the R&B models, the signed transition rates are close to 0, signifying a balance between clockwise and counterclockwise transitions between neighboring wells.

The shape of the torsional potential expression has a clear effect on the simulated transition rates. The higher transition rates exhibited by the R&B systems can be attributed to the difference between the *gauche* to *trans* barriers (see

TABLE IV. Average transition rates (ATR) per torsional angle.<sup>a</sup> Definition A.

System	ATR (Steele) (ps <sup>-1</sup> )	ATR (R&B) (ps <sup>-1</sup> )	ATR <sub>R&amp;B</sub> /ATR <sub>Steele</sub>
<i>S</i> <sub>1</sub>	0.0584	0.0851	1.46
<i>S</i> <sub>2</sub>	0.0529	0.0774	1.46
<i>S</i> <sub>3</sub>	0.0436	0.0688	1.57
<i>L</i> <sub>1</sub>	0.0597	0.0951	1.59
<i>L</i> <sub>2</sub>	0.0511	0.0807	1.58
<i>L</i> <sub>3</sub>	0.0448	0.0559	1.25

<sup>a</sup>Standard deviation does not exceed  $5 \cdot 10^{-4}$  for systems *S*<sub>1</sub>, *S*<sub>2</sub>, *S*<sub>3</sub>, and  $1.5 \cdot 10^{-3}$  for systems *L*<sub>1</sub>, *L*<sub>2</sub>, and *L*<sub>3</sub>.



TABLE V. Average transition rates per torsional angle (ATR).<sup>a</sup> Definition B.

System	ATR (Steele)(ps <sup>-1</sup> )	ATR (R&B)(ps <sup>-1</sup> )	ATR <sub>R&amp;B</sub> /ATR <sub>Steele</sub>
<i>S</i> <sub>1</sub>	0.0483	0.0628	1.30
<i>S</i> <sub>2</sub>	0.0424	0.0560	1.32
<i>S</i> <sub>3</sub>	0.0337	0.0492	1.46
<i>L</i> <sub>1</sub>	0.0514	0.0726	1.41
<i>L</i> <sub>2</sub>	0.0395	0.0565	1.43
<i>L</i> <sub>3</sub>	0.0317	0.0374	1.18

<sup>a</sup>Standard deviation does not exceed  $5 \times 10^{-4}$  for systems *S*<sub>1</sub>, *S*<sub>2</sub>, *S*<sub>3</sub>, and  $1.5 \times 10^{-3}$  for systems *L*<sub>1</sub>, *L*<sub>2</sub>, and *L*<sub>3</sub>.

Table II) associated with the Steele and R&B expressions. A rough estimate of the difference in transition rates may be calculated through the ratio

$$\frac{P_{\text{R\&B}}(t \leftrightarrow g^{\pm})}{P_{\text{Steele}}(t \leftrightarrow g^{\pm})} = e^{(\Delta E_{\text{Steele}} - \Delta E_{\text{R\&B}})/k_B T} \approx 1.5, \quad (6)$$

where  $\Delta E$  refers to the *gauche* to *trans* barrier. The proportionality constant between the R&B and Steele transition rates (Table V) is in close agreement with this factor.

The above discussion applies for results produced from an analysis using transition definition B or transition definition A with  $\pm 20$  deg windows. However, important differences within the transition statistics arise when the width of the window within definition A is varied. For instance, in system *L*<sub>2</sub> (Table I), narrowing the wells to  $\pm 10$ ,  $\pm 5$ , or  $\pm 2$  deg symmetrically around the minima resulted in transition rates reduced (as compared to the  $\pm 20$  well widths) by factors of 1.17, 1.45, and 2.35, respectively. Therefore, it is clear that the respective transition definitions must be explicitly taken into account when comparisons between different literature values are to be made.

## 2. Torsion coupling analysis

The cooperative nature of conformational motion is a key element in the localization of segmental polymer dynamics. These motions have been addressed within simulation studies of a variety of polymeric systems in vacuum, solution, and the bulk.<sup>15–27</sup> Comparison between isolated PE chains and melts<sup>15</sup> showed an enhanced conformational change correlation in the melt state; moderate for second neighbors but significantly higher for self-correlations. In a PI system, it was again found that in the melt environment the probability of second neighbor correlations is higher compared to the solution state.<sup>18</sup> In the present study we methodically examine the torsional coupling for the PE systems of Table I, assessing the relative contribution of the different factors (density, torsional potential, chain length) to the conformational cooperativity.

Several analysis methods have been developed to explore these motions in greater detail.<sup>15,16,24,28–30</sup> In the present case, the trajectories have been analyzed by a method due to Moe and Ediger.<sup>16</sup> This technique focuses on a torsional angle undergoing a conformational transition and observes how the neighboring torsional angles of the same

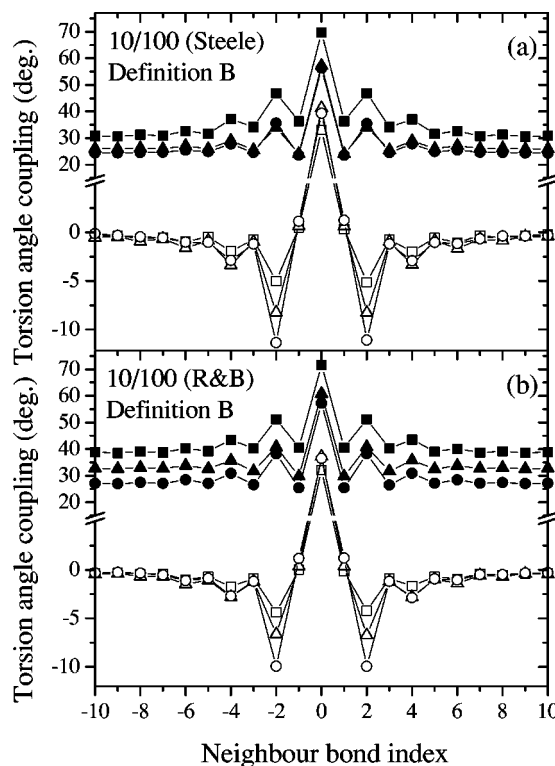


FIG. 6. Torsion angle coupling for the 10/100 systems, at all the examined densities ( $\square$ ,  $\blacksquare$   $\rho=0.29$  g/cm<sup>3</sup>,  $\blacktriangle$ ,  $\triangle$   $\rho=0.59$  g/cm<sup>3</sup>,  $\circ$ ,  $\bigcirc$   $\rho=0.79$  g/cm<sup>3</sup>) in systems simulated with the Steele (a) and R&B (b) torsional potentials, when a transition follows definition B. The filled and open symbols represent the nondirectional and the directional cases, respectively.

polymer chain respond to this triggering transition (TT). The average change of a torsional angle  $\phi$  in response to a TT is calculated as

$$\langle A(\Delta\phi_i) | \phi_i(\tau_{\text{trans}} + \Delta t) - \phi_i(\tau_{\text{trans}} - \Delta t) \rangle, \quad (7)$$

where  $A(\Delta\phi_i)$  assumes the values of  $\pm 1$ , for torsional motion in the same (+) or opposite (−) direction as the TT. This comparison can be done as a function of time after the triggering transition by varying  $\Delta t$  and as a function of distance along the chain backbone by performing the analysis for first neighbor torsional angles,  $\Delta\phi_i \pm 1$ , second neighbor torsional angles,  $\Delta\phi_i \pm 2$ , etc. The generic characteristics of the observed coupling pattern proved to be independent of whether definition A or B was used to define the TT. Therefore, only plots using the B definition are shown.

Figures 6(a), 6(b), 7(a), and 7(b) illustrate these plots for the 10/100 and the 50/20 systems, respectively. The value of  $\Delta t$  is fixed at 1 ps throughout this analysis. The filled symbols represent the nondirectional (NDR) version of expression (7) when the sign of  $\Delta\phi$  is not considered (i.e.,  $A$  is taken to be 1). The open symbols depict the directional (DR) case of expression (7) where the sign of the rotation for  $\Delta\phi$  is considered relative to the direction of the TT. The lines are aids to the eye. The analysis is carried out up to the fifth neighbors for the 50/20 systems and up to the tenth neighbors for the 10/100 systems. The triggering transition is indexed as 0.

Concentrating first on the filled symbols within Fig. 6(a) for the Steele torsional angles, a second and much more re-

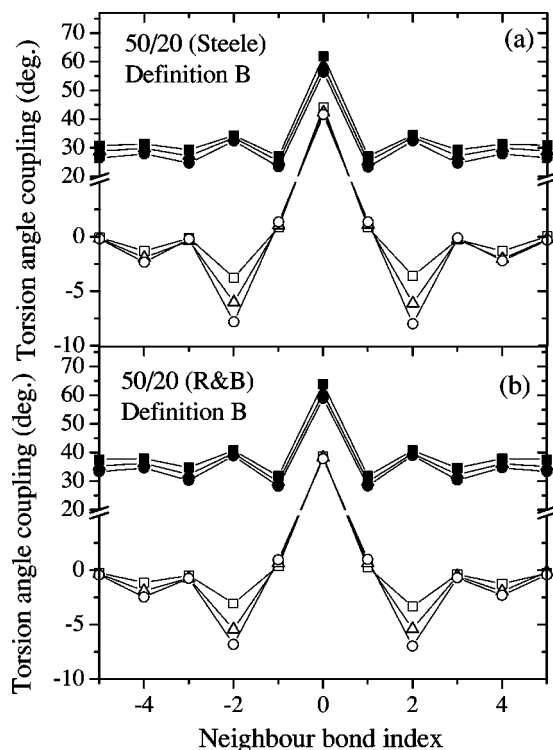


FIG. 7. Torsion angle coupling for the 50/20 systems, at all the examined densities ( $\square$ ,  $\blacksquare$   $\rho=0.29$  g/cm<sup>3</sup>,  $\blacktriangle$ ,  $\triangle$   $\rho=0.59$  g/cm<sup>3</sup>,  $\bullet$ ,  $\circ$   $\rho=0.70$  g/cm<sup>3</sup>) in systems simulated with the Steele (a) and R&B (b) torsional potentials, when a transition follows definition B. The filled and open symbols represent the nondirectional and the directional cases, respectively.

duced level of fourth neighbor coupling is observed in both the NDR and DR cases. Beyond the fourth neighbor peak, there is slight evidence for sixth neighbor coupling followed by a “background level” (BL) of 25 to 30 deg in the magnitude of NDR coupling. The R&B BL is generally higher than in the Steele systems, except for the highest density 10/100 case where the R&B and Steele backgrounds are similar. The observed difference in the BL is consistent with the approximately 7 deg difference in the location of the gauche minima between the two torsional potential expressions. The background level of the Steele and R&B DR plots plateaus at 0, indicating a balance between the clockwise and the counterclockwise torsional angle rotations relative to the TT. The DR plots within Figs. 6(a) and 6(b) reveal that this coupling is counter-rotational relative to the rotational sense of the TT.

Density seems to increase the relative magnitude of the second neighbor coupling with respect to each BL within the NDR plots. This effect is clearly evident within the DR plots where all the background levels collapse together. For the 50/20 systems (Fig. 7) the relative intensity of NDR and DR second and fourth neighbor coupling is slightly reduced relative to the analogous 10/100 cases [compare Fig. 6(a) to 7(a) and Fig. 6(b) to 7(b)]. A quantitative analysis of the coupling amplitudes (see Table VI) reveals that for both chain lengths and torsional potentials, the magnitude of the second neighbor coupling has increased by more than a factor of 2 when comparing the lower to the higher density. Roughly similar relative behavior is observed for fourth neighbor coupling

TABLE VI. Torsional coupling amplitudes (deg)<sup>a</sup>. Definition B.

System	2nd Neighbor		4th Neighbor	
	Steele	R&B	Steele	R&B
$S_1$	3.77	3.06	1.31	1.15
$S_2$	6.03	5.44	1.93	1.90
$S_3$	7.82	6.83	2.35	2.48
$L_1$	5.03	4.39	1.95	1.73
$L_2$	8.24	6.63	3.37	2.90
$L_3$	11.37	9.93	2.79	2.70

<sup>a</sup>Estimated error, does not exceed 0.50 deg for systems  $S_1$ ,  $S_2$ ,  $S_3$ , and 0.63 deg for systems  $L_1$ ,  $L_2$ , and  $L_3$ .

for the 50/20 chains. However, the low levels of fourth neighbor coupling in the 10/100 cases peak at the intermediate density.

As found for the transition rates, the transition definition affects the degree of coupling as well. Narrowing of the wells in definition A, to  $\pm 10$ ,  $\pm 5$ , or  $\pm 2$  deg symmetrically around the minima for system  $L_2$ , results in a decrease of the amplitude of the second neighbor coupling by factors of 1.14, 1.26, and 1.34, respectively.

#### IV. DYNAMICS

The dynamic response of the simulated systems was investigated through the second ( $P_2$ ) Legendre polynomial autocorrelation functions (ACFs)<sup>31</sup> involving the *torsional angle*  $P(\phi(t))$  in addition to the  $i$ th repeat unit based *bisector*  $\mathbf{s}_i$ , *out of plane*  $\mathbf{o}_i$ , the *bond*  $\mathbf{b}_i$ , and *chord*  $\mathbf{c}_i$  vectors. These vectors are constructed from the laboratory-based unfolded coordinates,  $\mathbf{r}_i$ , as indicated in the following equations:

$$\mathbf{b}_i = \frac{\mathbf{r}_{i+1} - \mathbf{r}_i}{|\mathbf{r}_{i+1} - \mathbf{r}_i|}, \quad (8)$$

$$\mathbf{c}_i = \frac{\mathbf{b}_i + \mathbf{b}_{i+1}}{|\mathbf{b}_i + \mathbf{b}_{i+1}|}, \quad (9)$$

$$\mathbf{o}_i = \frac{\mathbf{b}_i \times \mathbf{b}_{i+1}}{|\mathbf{b}_i \times \mathbf{b}_{i+1}|}, \quad (10)$$

$$\mathbf{s}_i = \frac{\mathbf{b}_{i+1} - \mathbf{b}_i}{|\mathbf{b}_{i+1} - \mathbf{b}_i|}, \quad (11)$$

$$P(\phi(t)) = \frac{\langle \cos(\phi(t)) \cos(\phi(0)) \rangle - \langle \cos(\phi(0)) \rangle^2}{\langle \cos(\phi(0)) \cos(\phi(0)) \rangle - \langle \cos(\phi(0)) \rangle^2}. \quad (12)$$

The correlation functions are analyzed using the CONTIN<sup>32,33</sup> algorithm, which represents their decay as a continuous distribution of exponential processes defined by Eq. (13)

$$C(t) = \int_0^\infty F(\ln(\tau)) e^{-t/\tau} d \ln \tau, \quad (13)$$

where  $F(\ln(\tau))$  symbolizes the normalized *distribution of relaxation times* (DRT). No *a priori* assumption is made regarding the form of the correlation functions except that they can be represented by a continuous superposition of exponentials. CONTIN is extensively used for analysis of experimental results<sup>34,35</sup> and has been proven to be a very powerful

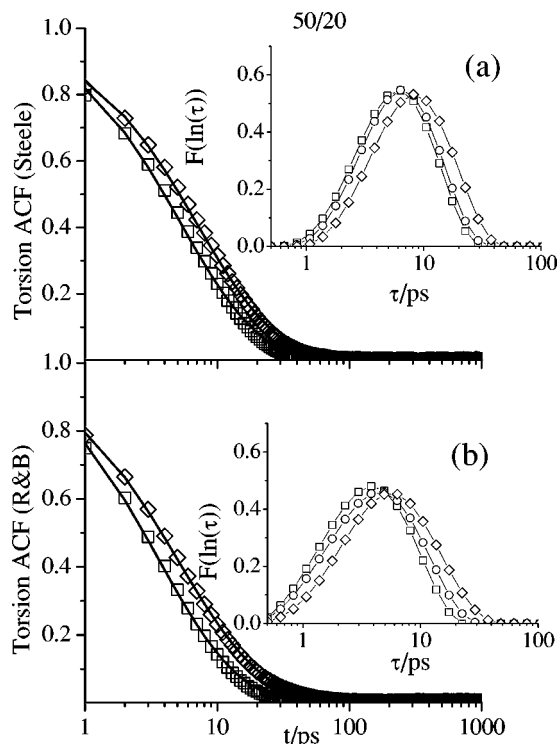


FIG. 8. Torsion autocorrelation functions for the 50/20 systems simulated with the Steele (a) and the R&B (b) torsional potentials, for densities  $\rho=0.29$  g/cm<sup>3</sup>  $\square$ ,  $\rho=0.70$  g/cm<sup>3</sup>  $\diamond$ . For clarity purposes, the torsional correlation functions are not shown for  $\rho=0.59$  g/cm<sup>3</sup>. The solid lines through the points represent the fit resulting from the CONTIN analysis, while the insets ( $\circ$  for  $\rho=0.59$  g/cm<sup>3</sup>) show the distribution of relaxation times for the corresponding densities.

tool that is particularly effective in identifying individual relaxation processes within a dynamic spectra.<sup>36</sup> This analysis method was earlier employed<sup>37</sup> in a simulation study where the distribution of rotational diffusion coefficients for individual bonds was calculated from  $P_1$  and  $P_2$  spectra. The authors found an inconsistency in the distributions calculated from the equations analogous to Eq. (13) when different kernels were used for the description of  $P_1$  and  $P_2$  ACFs. In our case we calculate the distribution of relaxation times with the same exponential kernel [Eq. (13)] for all the ACFs.<sup>38</sup>

### A. Torsional ACF

The torsional ACF [Eq. (12)], expressing the degree of correlation of the internal rotations,<sup>39</sup> is shown for the 50/20 systems for the Steele [Fig. 8(a)] and the R&B [Fig. 8(b)] potentials for the simulated densities. The lines through the points are produced from CONTIN analysis of the data while the insets depict the corresponding DRTs. Error bars for the data which comprise a DRT inset do not exceed the plotted symbol size. The abscissa is presented in logarithmic scale and the first point of all the ACFs was omitted in the fitting procedure due to the lack of resolution in the decay below 1 ps. A characteristic relaxation time (CRT) for the correlation functions can be estimated from the location of the maxima for the corresponding DRTs, while broader distributions de-

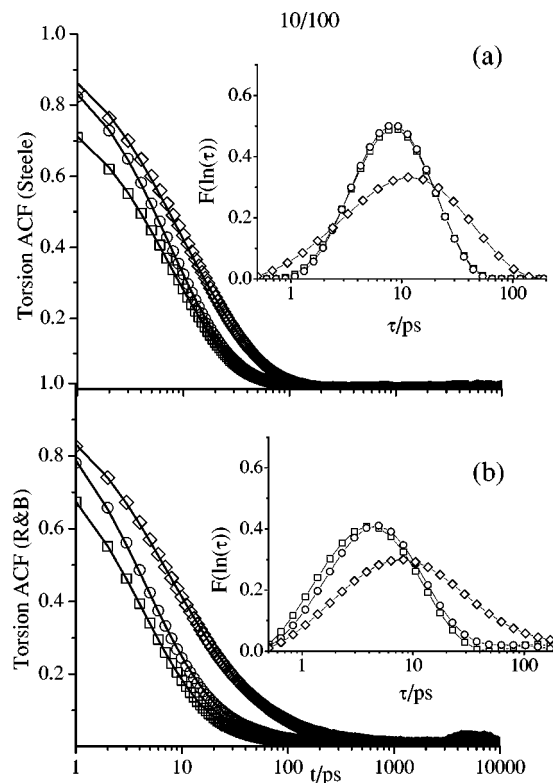


FIG. 9. Torsion autocorrelation functions for the 10/100 systems simulated with the Steele (a) and the R&B (b) torsional potentials, for all the examined densities ( $\square$   $\rho=0.29$  g/cm<sup>3</sup>,  $\circ$   $\rho=0.59$  g/cm<sup>3</sup>,  $\diamond$   $\rho=0.79$  g/cm<sup>3</sup>). The solid lines through the points represent the fit resulting from the CONTIN analysis, while the insets show the distribution of relaxation times for the corresponding densities.

note a larger dispersion of exponential relaxation modes as described in Eq. (13). Analogous pictures for the 10/100 systems, are shown in Figs. 9(a) and 9(b).

The CRTs for the 50/20 and 10/100 systems reveal the correlation functions for the R&B potential decorrelate faster than their Steele counterparts, in agreement with the observed transition rates, with the R&B DRTs being slightly broader than the Steele DRTs. For the lowest two densities using the same torsional potential, the 50/20 and the 10/100 systems decay with approximately the same CRT. At the highest density studied, the CRTs for the 50/20 systems shift to slightly longer times but the shapes remain similar to their lower density analogs. The CRTs for the 10/100 systems also shift slightly to longer times with the most noticeable difference being an increase in the width of their DRTs. This shift, and the broadening of the DRTs at higher density, is consistent with more restrained and collective torsional motions.

### B. Geometric ACF

Figures 10(a) and 10(b) illustrate the  $P_2$  ACFs for the vectors described by Eqs. (8) through (11) using the Steele torsional potential at the intermediate density  $\rho=0.59$  g/cm<sup>3</sup>. As shown from previous investigations of PE chains either as isolated<sup>31</sup> or in bulk conditions,<sup>40</sup> the out-of-plane and bisector vectors decorrelate in a very similar manner, and faster than the bond and chord vectors which are more oriented along the chain backbone. The same behavior is observed for all the examined densities, the two chain lengths, and the R&B analogs.



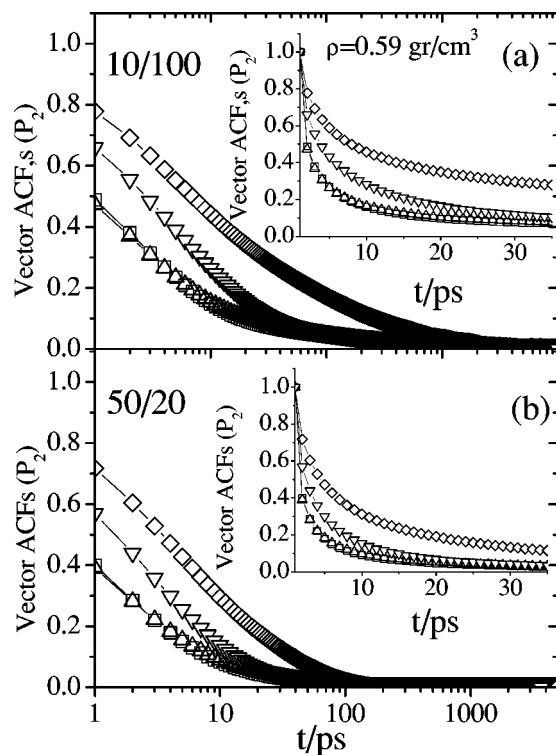


FIG. 10.  $P_2$  autocorrelation functions for the 10/100 (a) and 50/20 (b) systems, simulated with the Steele torsional potential, for the intermediate density  $\rho=0.59$  g/cm<sup>3</sup>. Vectors bisector  $\square$ , out-of-plane  $\triangle$ , chord  $\diamond$ , bond  $\nabla$  are shown for comparison. Their early time decay is shown in linear plots as insets.

Figures 11(a), 11(b), 12(a), and 12(b) display the relaxational characteristics ( $P_2$  ACFs) of the bond (a) and chord (b) vectors, for the 50/20 and the 10/100 systems, respectively. The log-log plot format is chosen for a better visual identification of the features that will be discussed forthwith. The Steele models are represented by line patterns, with the R&B models denoted by symbols. The solid thick curves in Figs. 11(a) and 12(a) serve as a reference to the behavior of a single exponential decay. The exponential process appears as a line of single curvature with the length of the plateau increasing as the time constant is increased. Relative to a single exponential decay with time constant  $\tau$ , processes of a stretched exponential type ( $C(t) \propto e^{-(t/\tau)^\beta}$ ,  $0 < \beta < 1$ ) with the same time constant  $\tau$  would exhibit a less steep decorrelation but still with a single curvature. Semilogarithmic plots of the  $P_2$  ACFs for the Steele bond (a) and chord (b) vectors for the 10/100 and 50/20 systems are shown in Figs. 13 and 14, respectively. The lines through each set of data points represent results from CONTIN analysis where the corresponding DRTs are included as insets to each figure. The resulting fits from this analysis (represented by the solid lines through the points of the corresponding ACFs) seem to capture the average behavior of the correlation functions, even at the long time regimes where the statistics are poorer.

Figure 11 reveals the  $P_2$  ACFs for the bond and the chord vectors of the 50/20 system. Both decay at the earliest examined times, in a nonexponential manner, with a quicker decay being observed for the R&B systems. Increasing density slows the decay of these ACFs, with slight changes in

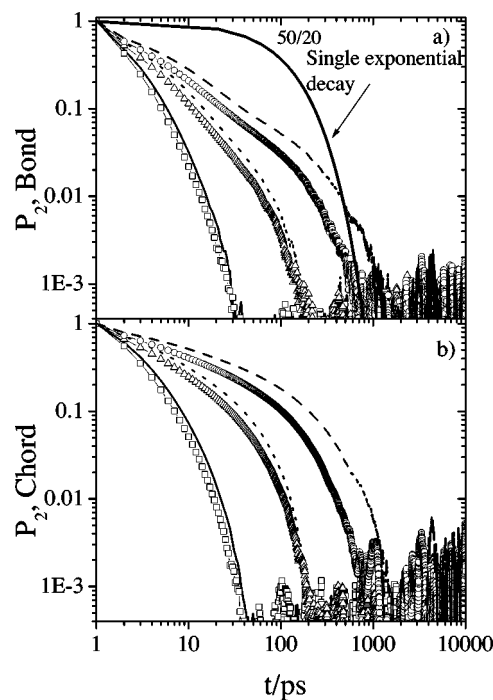


FIG. 11.  $P_2$  bond (a) and chord (b) autocorrelation functions for the 50/20 models, simulated by the Steele (lines) and R&B (symbols) torsional potentials, for all the examined densities:  $\square$   $\rho=0.29$  g/cm<sup>3</sup>,  $\triangle$   $\rho=0.59$  g/cm<sup>3</sup>, and  $\circ$  for  $\rho=0.70$  g/cm<sup>3</sup>. The thick solid curve (upper figure) shows the behavior of a single exponential decay, with time constant  $\tau=100$  ps.

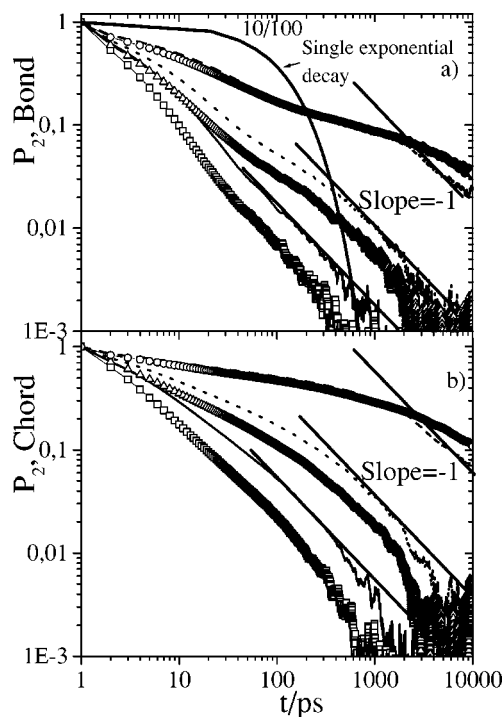


FIG. 12.  $P_2$  bond (a) and chord (b) autocorrelation functions for the 10/100 systems, simulated by the Steele (lines) and R&B (symbols) torsional potentials, for all the examined densities:  $\square$   $\rho=0.29$  g/cm<sup>3</sup>,  $\triangle$   $\rho=0.59$  g/cm<sup>3</sup>, and  $\circ$  for  $\rho=0.79$  g/cm<sup>3</sup>. The thick solid curve (upper figure) shows the behavior of a single exponential decay, with time constant  $\tau=100$  ps.

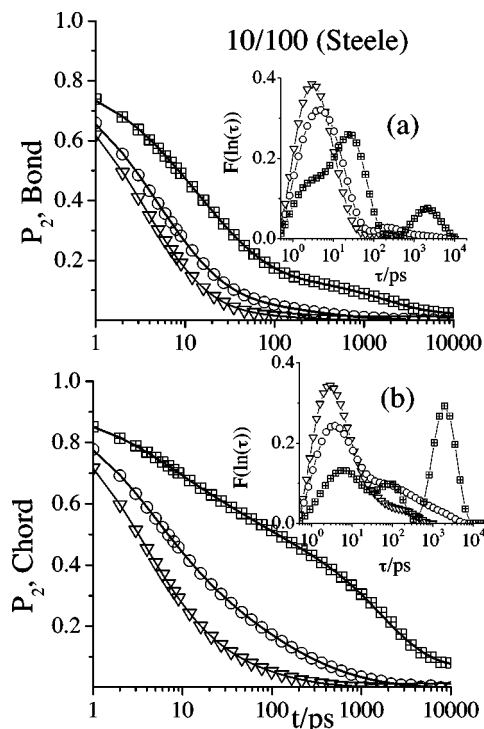


FIG. 13.  $P_2$  bond (a) and chord (b) autocorrelation functions for the 10/100 systems, simulated by the Steele torsional potential, for all the examined densities:  $\nabla$   $\rho=0.29$  g/cm<sup>3</sup>,  $\circ$   $\rho=0.59$  g/cm<sup>3</sup>, and  $\boxplus$ , for  $\rho=0.79$  g/cm<sup>3</sup>. The solid lines through the points represent the fit resulting from the CONTIN analysis.

curvature observed around 100 to 200 ps. Similar behavior is observed in Fig. 12 for the  $P_2$  ACFs for the bond and the chord vectors of the 10/100 system. However, curvature changes within the ACF decays are much more evident relative to the 50/20 system, especially at the highest density. The nonexponential decay of these ACFs is emphasized by the shape of their DRTs as depicted in Figs. 13 and 14.<sup>41</sup> As density increases, the early time portion of each DRT for each ACF decreases in amplitude and the peak moves to slightly longer times. This region of the decay of the ACFs can be attributed to the segmental process,<sup>40,42–44</sup> which involves the reorientational motions of chain segments on the length scale of few bonds. The late-time regime is characterized by the appearance of slower processes which possess DRT peaks which grow in amplitude and also move to longer time upon densification. Within the DRT for the most dense 10/100 systems [i.e.,  $\boxplus$  symbols in insets of Figs. 13(a) and 13(b)], it is interesting to note the evolution of an additional *intermediate* mode on a time scale between that of the segmental and long-time dynamics. It must be noticed that this process appears on a time scale [CRT $\approx$ 100 ps, see the inset of Fig. 13(b)] where the quality of the statistics allows a reliable calculation of the ACFs and the corresponding DRTs.

Relaxation processes slower than the segmental have been suggested to arise from contributions of longer length-scale motions<sup>45–49</sup> to the local dynamic response. As proposed in the case of melts,<sup>40</sup> this behavior can be thought to originate from an effective “*pipe*” formed from the surrounding chains constraining the relaxation of the chain axis,

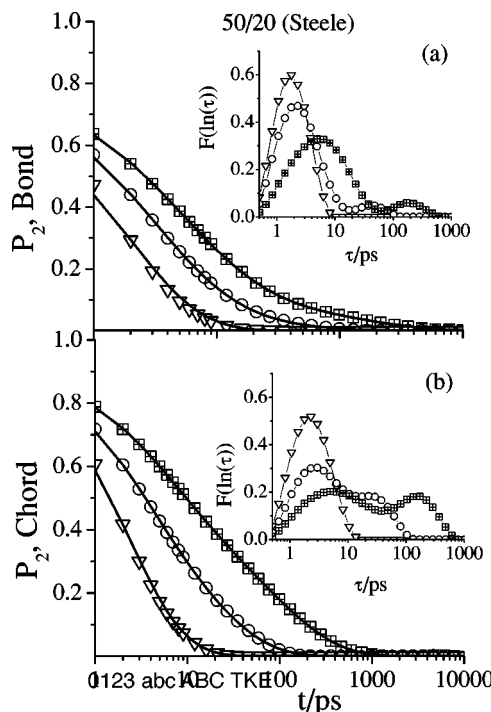


FIG. 14.  $P_2$  bond (a) and chord (b) autocorrelation functions for the 50/20 systems, simulated by the Steele torsional potential, for all the examined densities:  $\nabla$ ,  $\rho=0.29$  g/cm<sup>3</sup>,  $\circ$ ,  $\rho=0.59$  g/cm<sup>3</sup>, and  $\boxplus$ , for  $\rho=0.70$  g/cm<sup>3</sup>. The solid lines through the points represent the fit resulting from the CONTIN analysis.

even after the correlation of the torsional angles is lost. This effect is not to be confused with the “*tube*” model<sup>14</sup> associated with chain reptation. The long-time behavior of the  $P_2$  ACFs for the bond and chord vectors of the 10/100 models (described by the slowest peaks in the respective DRTs) is consistent<sup>46,50</sup> with Rouse-like<sup>51</sup> dynamics which scale as  $P_2(t) \propto t^{-1}$  [i.e., slope of  $-1$  in Figs. 12(a) and 12(b)]. However, description of the short-scale high-wave-vector dynamics based solely on the Rouse model proved inadequate.<sup>50,52</sup>

This work suggests local dynamics should be analyzed in terms of separate motional processes on both short *and* longer time scales.

### C. Distribution of orientational angles

In order to gain more insight into the motion responsible for the relaxation of the geometric ACFs, we have investigated the distribution plots of the corresponding orientational angles. Function  $P(\Delta\theta(\Delta\tau))$  corresponds to the distribution of  $\Delta\theta(\Delta\tau)$ ,

$$\Delta\theta(\Delta\tau) = \langle \cos^{-1}(\mathbf{n}_{ik}(t) \cdot \mathbf{n}_{ik}(t + \Delta\tau)) \rangle, \quad (14)$$

where  $\mathbf{n}_{ik}(t)$  is the  $i$ th unit vector of the  $k$ th chain, at time  $t$  in the direction of one of the local vectors [Eqs. (8)–(11)].  $\Delta\tau$  is the time step by which we sample the change in angle,  $\Delta\theta$ . The average  $\langle \rangle$  is taken first over all the consecutive trajectory points separated by  $\Delta\tau$ , then over all the considered vector indices  $i$ , and finally over all the chains. For this analysis, the 10/100 and 50/20 systems produced similar results, so only data from the larger systems are illustrated. Figure 15 presents plots for the chord, bond, bisector, and

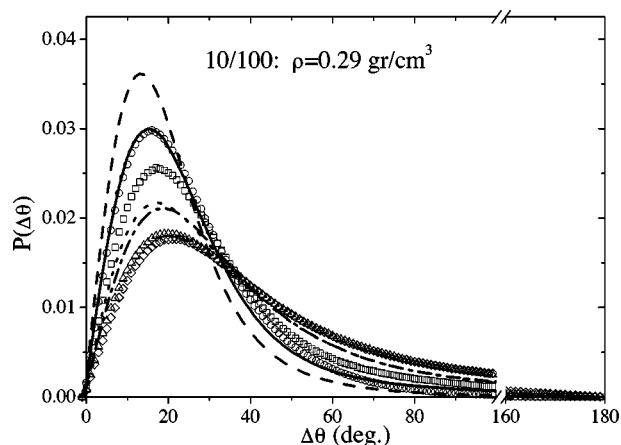


FIG. 15. Reorientation angle distributions for the 10/100 systems, at  $\rho = 0.29 \text{ g/cm}^3$ , simulated with the Steele (line patterns), and R&B (symbols) torsional potentials, for all the examined local vectors for  $\Delta\tau = 1 \text{ ps}$ : chord (dashed line,  $\circ$ ), bond (solid line,  $\square$ ), bisector (dotted line  $\triangle$ ), and out-of-plane (dashed-dotted line  $\diamond$ ) vectors.

out-of-plane vector for both the Steele (lines) and R&B (symbols) systems at the density  $\rho = 0.29 \text{ g/cm}^3$  and  $\Delta\tau = 1 \text{ ps}$ . For a given torsional potential, the chord and bond vector distribution plots illustrate the narrowest distributions and

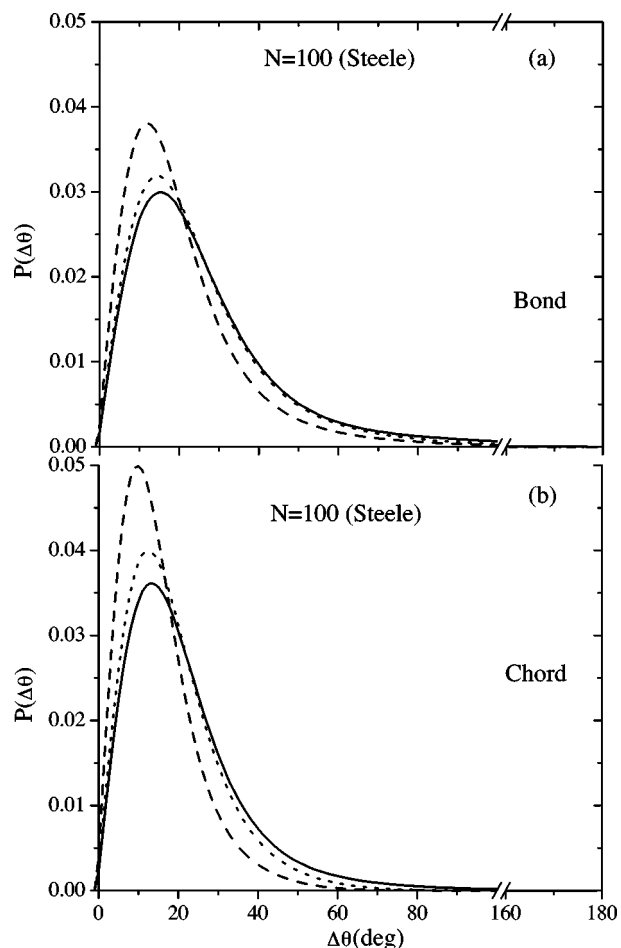


FIG. 16. Reorientation angle distributions for the bond (a) and chord (b) vectors, for 10/100 systems, simulated with the Steele torsional potential, with  $\Delta\tau = 1 \text{ ps}$ , in all the examined densities: solid line for  $\rho = 0.29 \text{ g/cm}^3$ , dotted line for  $\rho = 0.59 \text{ g/cm}^3$ , and dashed line for  $\rho = 0.79 \text{ g/cm}^3$ .

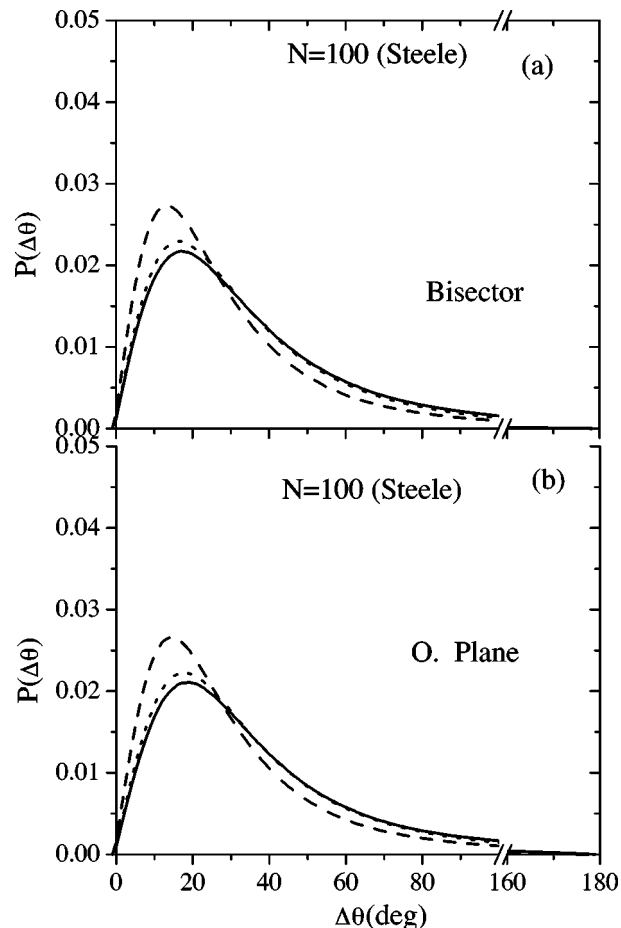


FIG. 17. Reorientation angle distributions for the bisector (a) and out of plane (b) vectors, for 10/100 systems, simulated with the Steele torsional potential, with  $\Delta\tau = 1 \text{ ps}$ , in all the examined densities: solid line for  $\rho = 0.29 \text{ g/cm}^3$ , dotted line for  $\rho = 0.59 \text{ g/cm}^3$ , and dashed line for  $\rho = 0.79 \text{ g/cm}^3$ .

highest peak amplitudes located at smaller  $\Delta\theta$  relative to the out-of-plane and bisector plots. The broad shape of the out-of-plane and bisector plots with peak values occurring at higher values of  $\Delta\theta$  implies more reorientational freedom relative to the more restrained motion conveyed by the narrow plots for the bond and chord vectors. This line of reasoning is also applicable when comparing the Steele and R&B distribution plots for a given vector. The R&B distributions are slightly broader and possess peak amplitudes which are smaller than their Steele counterparts. This broad nature, combined with the lower-peaked  $\Delta\theta$  distributions, would imply faster R&B dynamics relative to Steele dynamics, which is consistent with the transition rates presented in Tables V and IV, the torsional ACFs presented in Figs. 8 and 9, and the bond and chord ACFs presented in Figs. 11 and 12.

Figures 16(a), and 16(b) describe the angular distributions, for the *bond* (a), and the *chord* (b) vectors, as a function of density. The analogous distributions for the bisector and the out-of-plane vectors, are shown in Figs. 17(a) and 17(b), respectively. As density increases, each distribution becomes narrower with peak positions shifting to lower  $\Delta\theta$  values. Figure 18 illustrates the behavior of the  $P(\Delta\theta(\Delta\tau))$  plots for the chord vector of the 10/100 Steele chains as the

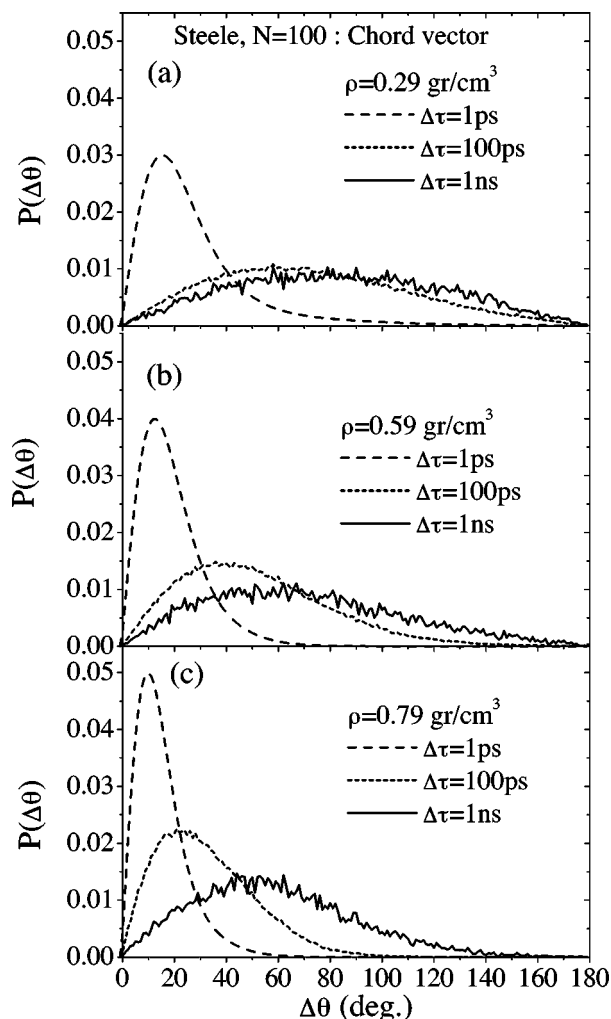


FIG. 18. Reorientation angle distributions for the chord vector of the 10/100 systems, simulated with the Steele torsional potential, in all the examined densities (a)  $\rho=0.29$  g/cm<sup>3</sup>, (b)  $\rho=0.59$  g/cm<sup>3</sup>, and (c)  $\rho=0.79$  g/cm<sup>3</sup> for three different time steps:  $\Delta\tau=1$  ps (dashed line),  $\Delta\tau=100$  ps (dotted line), and  $\Delta\tau=1$  ns (solid line).

value of  $\Delta\tau$  is increased. At lower density, as shown in Fig. 18(a), the curves are very broad and roughly symmetric about 90 deg at  $\Delta\tau$  values around 100 ps, at which time the  $P_2$  ACF for the chord vector has nearly decayed to zero in Fig. 13(b). The decay of chord vector ACFs slowed dramatically as density was increased, which in Fig. 18(c) corresponds to  $P(\Delta\theta(\Delta\tau))$  curves which are much more asymmetric and peaked at lower values of  $\Delta\theta$  relative to their low-density analogs. This behavior demonstrates that orientational memory at higher densities is apparently retained on time scales of the order of the overall chain motion. Hence, it accounts for the slow modes observed in the decorrelation of the associated vector's ACFs.

## V. SUMMARY

Molecular dynamics simulations of linear united atom polyethylene models were performed for a systematic investigation of local conformational statistics and dynamics as a function of density. At each density, the effect on the simulated local dynamics on chain length, the shape of the input

torsional potential expression, and the definition of a conformational transition were also analyzed. As intermolecular congestion increases with increasing density, the torsional transition rates decrease with simultaneous increases in torsional angle coupling amplitude and a broadening of the torsional ACFs' spectra (for the 10/100 system only). The coupling amplitudes are observed to be dependent on the chain length, and to a lesser extent on the parametrization of the torsional angle potential.

DRT analysis of geometric autocorrelation functions constructed from repeat unit-based vectors illustrated at least two peaks at all densities and chain lengths studied. One peak corresponds to a fast segmental mode (less than 10 ps) whose intensity decreases with increasing density. A second peak is observed at much longer times with an intensity that increases within increasing density. It is only for the 10/100 system at the highest simulated density that a third intermediate peak develops at approximately 100 ps. The absence of this process in local dynamic spectra from the 50/20 systems even at the highest density, as well as from the 10/100 systems at the lower densities, signifies that its appearance should be attributed in the combined effect of density and chain length. Examination of dynamics on length scales of the order of the end-to-end vector showed that this process remains absent from the short chain spectra, while it appears in the two higher densities for the long chain systems. Further analysis for the spectral characteristics of the slower modes will be presented in a separate work.

A route towards a better understanding of the observed dynamic behavior is offered through the examination of the respective angular distributions. For a given time resolution,  $\Delta\tau$ , increasing density affords narrower and lower  $\Delta\theta$  peaked distributions, implying a more constrained and essentially slower reorientation. At constant density, examination of the distributions at increasing time steps provides information on the characteristic time scale for loss of the orientational memory, which can be directly associated to the observed dynamic response. This "mapping" of the degree of orientational freedom experienced from the related vectors is therefore a particularly sensitive tool for probing modifications of local environment.

## ACKNOWLEDGMENTS

This work was supported by EPSRC Grant No. GR/L37021, and computer time was made available through the Joint Research Equipment Initiative scheme.

<sup>1</sup>S. Geyler and T. Pakula, *Makromol. Chem., Rapid Commun.* **9**, 617 (1988).

<sup>2</sup>S. Geyler, T. Pakula, and J. Reiter, *J. Chem. Phys.* **92**, 2676 (1990).

<sup>3</sup>T. Pakula, *J. Chem. Phys.* **95**, 4685 (1991).

<sup>4</sup>W. Hoover, *Phys. Rev. A* **31**, 1695 (1985).

<sup>5</sup>T. Forester and W. Smith, CCLRC, Daresbury Laboratory, Daresbury, Warrington Wa4 4AD, England. DL-POLY is a parallel molecular dynamics package developed at Daresbury Laboratory, and is a property of the Council for the Central Laboratory of the Research Councils (CCLRC) (1998).

<sup>6</sup>M. Allen and D. Tildesley, *Computer Simulation of Liquids* (Clarendon, Oxford, 1989).

<sup>7</sup>J.-P. Ryckaert, G. Cicciotti, and H. Berendsen, *J. Comput. Phys.* **23**, 327 (1977).



- <sup>8</sup>D. Steele, J. Chem. Soc., Faraday Trans. 2 **81**, 1077 (1985).
- <sup>9</sup>J-P. Ryckaert and A. Bellemans, Chem. Phys. Lett. **30**, 123 (1975).
- <sup>10</sup>D. Brown, J. Clarke, M. Okuda, and T. Yamazaki, J. Chem. Phys. **104**, 2078 (1996).
- <sup>11</sup>D. Brown, J. Clarke, M. Okuda, and T. Yamazaki, J. Chem. Phys. **100**, 1684 (1994).
- <sup>12</sup>V. Harmandaris, V. Mavrantzas, and D. Theodorou, Macromolecules **31**, 7934 (1998).
- <sup>13</sup>M. Mondello, G. Grest, E. Webb, and P. Peczak, J. Chem. Phys. **109**, 798 (1998).
- <sup>14</sup>M. Doi and S. Edwards, *The Theory of Polymer Dynamics* (Clarendon, Oxford, 1989).
- <sup>15</sup>R. Boyd, R. Gee, J. Han, and Y. Jin, J. Chem. Phys. **101**, 788 (1994).
- <sup>16</sup>N. Moe and M. Ediger, Macromolecules **29**, 5484 (1996).
- <sup>17</sup>R. Gee and R. Boyd, J. Chem. Phys. **101**, 8028 (1994).
- <sup>18</sup>N. Moe and M. Ediger, Polymer **37**, 1787 (1996).
- <sup>19</sup>D. Rigby and R. Roe, J. Chem. Phys. **89**, 5280 (1988).
- <sup>20</sup>P. Pant, J. Han, G. Smith, and R. Boyd, J. Chem. Phys. **99**, 597 (1993).
- <sup>21</sup>D. Rigby and R. Roe, J. Chem. Phys. **87**, 7285 (1987).
- <sup>22</sup>D. Rigby and R. Roe, Macromolecules **22**, 2259 (1989).
- <sup>23</sup>D. Rigby and R. Roe, Macromolecules **23**, 5312 (1990).
- <sup>24</sup>D. Adolf and M. Ediger, Macromolecules **24**, 5834 (1991).
- <sup>25</sup>J. Han, R. Gee, and R. Boyd, Macromolecules **27**, 7781 (1994).
- <sup>26</sup>E. Kim and W. Mattice, J. Chem. Phys. **101**, 6242 (1994).
- <sup>27</sup>R. Gee and R. Boyd, Comput. Theor. Polym. Sci. **8**, 93 (1998).
- <sup>28</sup>E. Helfand, Z. Wasserman, and T. Weber, Macromolecules **13**, 526 (1980).
- <sup>29</sup>J. Skolnick and E. Helfand, J. Chem. Phys. **72**, 5489 (1980).
- <sup>30</sup>C. Baysal, A. Atilgan, B. Erman, and I. Bahar, J. Chem. Soc., Faraday Trans. **91**, 2483 (1995).
- <sup>31</sup>T. Weber and E. Helfand, J. Chem. Phys. **87**, 2881 (1983).
- <sup>32</sup>S. Provencher, Comput. Phys. Commun. **27**, 229 (1982).
- <sup>33</sup>S. Provencher, in *Photon Correlation Techniques in Fluid Mechanics*, edited by E. O. Schulz-DuBois (Springer, Berlin, 1983).
- <sup>34</sup>T. Jian, S. Anastasiadis, A. Semenov, G. Fytas, K. Adachi, and T. Kotaka, Macromolecules **27**, 4762 (1994).
- <sup>35</sup>G. Fytas, K. Chrissopoulou, S. Anastasiadis, D. Vlassopoulos, and K. Karatasos, *Light Scattering and Photon Correlation Spectroscopy*, NATO ASI: 3. High Technology, Vol. 40, edited by E. R. Pike and J. B. Abbiss (Kluwer, New York, 1997).
- <sup>36</sup>All the DRTs presented henceforth are chosen among almost identical in terms of spectral characteristics (number, location, and shape of the peaks) solutions for  $F(\ln(\tau))$  [see Eq. (1)] possessing the minimum degree of information (i.e., number of peaks) absolutely necessary to describe the data.
- <sup>37</sup>R. Roe, D. Rigby, H. Furuya, and H. Takeuchi, Comput. Polym. Sci. **2**, 32 (1992).
- <sup>38</sup>It is a current issue of scientific debate whether the picture of the so-called "heterogeneous" or "homogeneous" scenario is more appropriate for the description of dynamics in the local segmental scale [see, for instance, Richter *et al.*, Phys. Rev. Lett. **82**, 1335 (1999), and references therein]. Here, we essentially adopt the heterogeneous picture, where local relaxation processes are expressed as a superposition of single exponentials, weighted by a distribution of relaxation times  $F(\ln(\tau))$ .
- <sup>39</sup>H. Takeuchi and K. Okazaki, J. Chem. Phys. **92**, 5643 (1990).
- <sup>40</sup>H. Takeuchi and R. Roe, J. Chem. Phys. **94**, 7446 (1991).
- <sup>41</sup>Fits to the ACFs of Fig. 14 by means of two stretched exponential functions (except for  $\rho=0.29$  g/cm<sup>3</sup>, where only one was utilized), resulted in stretched exponents ( $\beta$ ) for the fast process of:  $\beta_{\text{bond}}=0.74$ ,  $\beta_{\text{chord}}=0.74$  ( $\rho=0.29$  g/cm<sup>3</sup>),  $\beta_{\text{bond}}=0.67$ ,  $\beta_{\text{chord}}=0.63$  ( $\rho=0.59$  g/cm<sup>3</sup>) and  $\beta_{\text{bond}}=0.35$ ,  $\beta_{\text{chord}}=0.61$  ( $\rho=0.70$  g/cm<sup>3</sup>). Analogous fits for the 10/100 systems would require nine fitting parameters (three stretched exponents), rendering the uniqueness of the fit ambiguous.
- <sup>42</sup>R. Roe, J. Chem. Phys. **100**, 1610 (1993).
- <sup>43</sup>R. Roe, J. Non-Cryst. Solids **172-174**, 77 (1994).
- <sup>44</sup>A. Kopf, B. Dunweg, and W. Paul, J. Chem. Phys. **107**, 6945 (1997).
- <sup>45</sup>G. Smith, D. Yoon, and R. Jaffe, Macromolecules **28**, 5987 (1995).
- <sup>46</sup>W. Paul, G. Smith, and D. Yoon, Macromolecules **30**, 7772 (1997).
- <sup>47</sup>T. Pakula, K. Karatasos, S. Anastasiadis, and G. Fytas, Macromolecules **30**, 8463 (1997).
- <sup>48</sup>K. Kostov, K. Freed, E. Webb, M. Mondello, and G. Grest, J. Chem. Phys. **108**, 9155 (1998).
- <sup>49</sup>B. Ilan and R. Loring, Macromolecules **32**, 949 (1999).
- <sup>50</sup>W. Paul, G. Smith, D. Yoon, B. Farago, S. Rathgeber, A. Zirkel, L. Willner, and D. Richter, Phys. Rev. Lett. **80**, 2346 (1998).
- <sup>51</sup>P. Rouse, J. Chem. Phys. **21**, 1272 (1953).
- <sup>52</sup>D. Richter, M. Monkenbusch, J. Allgeier, A. Arbe, J. Colmenero, B. Farago, Y. Bae, and R. Faust, J. Chem. Phys. **111**, 6107 (1999).
- <sup>53</sup>R. Raff and J. Allison, *Polyethylene* (Interscience, New York, 1989).